Nano Research

Open Access

Research Article

Multifunctional graphene-containing hydrogel flexible strain sensor for intelligent sign language recognition and human motion detection

Kaiqi Zhang[1], Tiantian Yao[1], Dan Zhao[1], Yanan Li[1,2,3] ✉, Huitao Yu[1,2,3], Lina Jia[1,2,3], and Ruiguang Xing[1,2,3] ✉

[1] *School of Materials Science and Engineering, Inner Mongolia University of Science and Technology, Baotou 014010, China*
[2] *Inner Mongolia Key Laboratory of Advanced Ceramic Material and Devices, Baotou 014010, China*
[3] *Key Laboratory of Green Extraction & Efficient Utilization of Light Rare-Earth Resources (Inner Mongolia University of Science and Technology), Ministry of Education, Baotou 014010, China*

Cite this article: *Nano Research*, **2026**, *19*, 94908664. https://doi.org/10.26599/NR.2026.94908664

ABSTRACT: Hydrogels hold substantial promise for use in intelligent wearable devices that can translate gestures into recognizable signals. However, the practical deployment of conventional hydrogels is hindered by their inadequate mechanical robustness and poor environmental stability. To overcome these limitations, this study functionalized reduced graphene oxide (rGO) through amino-group modification (NH_2-rGO) and incorporated functionalized rGO and phytic acid (PA) into a polyvinyl alcohol (PVA) matrix to fabricate a PVA/PA/NH_2-rGO composite conductive hydrogel. The effects of PA and NH_2-rGO concentrations on the properties of the hydrogel were systematically investigated. The incorporation of a small amount of NH_2-rGO markedly improved the mechanical performance of the PVA/PA_4/NH_2-$rGO_{0.1}$ hydrogel, yielding a tensile strength of 0.7 MPa and an elongation at break of 305%. At the same time, dynamic hydrogen bonds within the network imparted the hydrogel with excellent cyclic durability. As non-toxic and environmentally benign components, NH_2-rGO and PA also contributed to enhanced conductivity, resulting in the high strain sensitivity of the composite hydrogel. Under both small (8%) and large (268%) strains, the hydrogel showed pronounced changes in relative electrical resistance, corresponding to a gauge factor of 2.38. Furthermore, a wearable strain sensor based on the prepared hydrogel accurately recognized gestures. Through the integration with machine learning algorithms, we developed a sign-language translation system capable of recognizing multiple gestures with high precision. This work provides a solid foundation for next-generation intelligent sign-language recognition technologies and offers broad potential for applications in human-machine interfaces, smart wearables, and the Internet of Things.

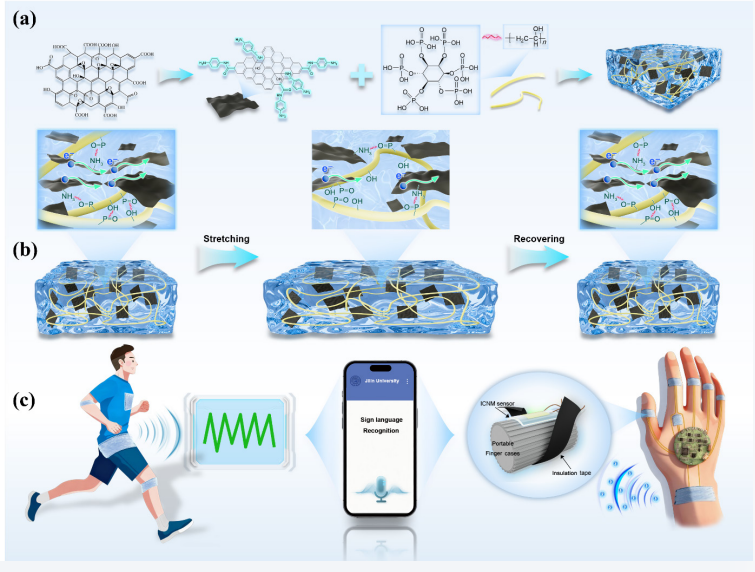

KEYWORDS: hydrogel, polyvinyl alcohol, amino-functionalized reduced graphene oxide, gesture recognition, flexible sensor

Received: December 31, 2025; **Revised:** March 4, 2026
Accepted: March 23, 2026

✉Address correspondence to Yanan Li, ynli2014@126.com; Ruiguang Xing, xingrg06@163.com

1 Introduction

The rapid development of artificial intelligence and the Internet of Things has brought notable advancements in human–machine interfaces and flexible electronic devices [1–4]. Flexible sensors have attracted increasing attention because of their broad applicability in

motion analysis [5], human–machine interaction [6], fall detection [7], and real-time medical monitoring [8–10]. To meet the application requirements of diverse scenarios, multiple sensor technologies have been extensively explored and applied in the research, development, and fabrication of flexible sensors [11–13]. Gesture-based wearable sensors, in particular, provide an intuitive means of interaction and enable the translation of hand gestures into interpretable signals. Owing to the refined mobility of human fingers, such sensors also enable reliable sign-language recognition, potentially offering crucial assistance for individuals with hearing impairments [14–16]. Among a wide range of sensing materials, hydrogels have emerged as promising candidates for smart wearable flexible sensors because of their tunable mechanical properties, structural softness, and high water content [17–19]. Moreover, hydrogel-based strain sensors integrated with machine-learning algorithms have been increasingly used for gesture recognition [20–23]. These sensors capture joint-motion patterns during hand movement and generate distinct electrical signals that correspond to specific gestures. Consequently, the development of hydrogel-based flexible sensors is central to sign-language recognition systems, as sensor performance directly determines the quality and resolution of the acquired signals.

For use as strain sensors, hydrogels must exhibit adequate electrical conductivity. Consequently, hydrogel-based strain sensors typically consist of a polymer hydrogel matrix and conductive fillers. Polyvinyl alcohol (PVA), a commonly used hydrogel matrix, offers several advantages over other materials, such as ease of preparation and functional modification, nontoxicity, hydrophilicity, and good biocompatibility. However, PVA also suffers from inherent drawbacks, including insufficient mechanical strength, limited electrical conductivity, poor environmental stability, and restricted electron-transport capability. Therefore, the development of hydrogel strain sensors with enhanced mechanical robustness and high sensitivity remains a considerable challenge. To improve the electrical conductivity properties of hydrogels, researchers have incorporated various conductive agents into them. Representative examples include polyaniline [24, 25], polypyrrole [26, 27], metal ions [27, 28], carbon nanotubes [29, 30], graphene [31, 32], and MXenes [32, 33], all of which have been employed to fabricate highly sensitive sensors with stable mechanical performance for continuous health monitoring. In addition, other polymers have been introduced to further enhance the performance of PVA-based hydrogels. For instance, Chen et al. combined demethylated lignin with PVA to synthesize a variety of PVA-based films, soft hydrogels, and rigid hydrogels with improved mechanical properties [34]. Hu et al. reported a PVA-based anisotropic hydrogel reinforced with polyaniline-encapsulated bacterial cellulose fibers, which maintained stable sensing accuracy at 200% strain [25]. Zhang et al. developed a soft–tough dual-layer gradient polyacrylamide/PVA/sodium alginate hydrogel, achieving high sensitivity and a broad stress-sensing range [35]. Nevertheless, the aforementioned conductive agents and polymer fillers still exhibit significant limitations, including high rigidity, poor solubility, and inherently low electrical conductivity (typically below 10 S/m at room temperature (18–25 °C), which is even lower when incorporated into hydrogels, falling far below the conductivity of graphene, 103–104 S/m). These shortcomings ultimately result in an uneven conductive network within the hydrogel. This not only hinders the formation of efficient conductive pathways but also increases the brittleness of hydrogels, making it difficult to balance electrical conductivity with stretchability.

Graphene has been widely investigated as a conductive material owing to its high specific surface area, good electrical conductivity, and intrinsic structural stability. However, graphene tends to agglomerate, with strong π–π interactions between graphene layers causing its stacking into large sheets during production and processing. This substantially reduces its effective surface area and conductivity [36]. The direct incorporation of graphene as a conductive filler into hydrogels also presents notable drawbacks. For example, Alam et al. prepared graphene/PVA composite hydrogel films using processable graphene sheets. Although graphene sheets effectively enhanced the electrical conductivity of the composite material, the effect was modest [37]. Shi et al. prepared PVA/graphene oxide (GO) composite hydrogels via the freeze-thaw method and evaluated the mechanical and tribological properties of hydrogels with different GO contents. The water-blocking effect of GO was reported to impede water permeation between PVA molecules [38]. Meng et al. fabricated oriented PVA/GO nanocomposite hydrogels with varying strain ratios. The PVA/GO sample at 200% strain exhibited enhanced mechanical properties owing to the formation of a microfibrillar structure, but the improvement was not substantial [39]. To overcome interlayer stacking and fully exploit the electrical conductivity and other advantages of graphene, functionalization strategies are commonly employed. Combining functionalized graphene with other polymers not only solves the problem of agglomeration encountered with pure graphene or GO but also enhances the mechanical flexibility, electrochemical stability, and ion-transport efficiency of composite hydrogels. Accordingly, graphene derivatives such as reduced GO (rGO) and functionalized graphene show broad application prospects in hydrogel-based electronic devices [40–42]. In our previous work, which served as a foundation for this study, we prepared polyacrylamide/amino-functionalized rGO (PAM/NH_2-rGO) hydrogels exhibiting good mechanical properties, electrical conductivity, sensing capabilities, and biocompatibility [43].

Herein, we successfully prepared PVA/PA/NH_2-rGO composite hydrogels by leveraging the hydrophilicity, chemical reactivity, environmental friendliness, and non-toxicity of amino-functionalized rGO (NH_2-rGO). As a conductive filler, NH_2-rGO provides abundant electron-conduction sites that facilitate the formation of continuous electronic pathways, thereby enhancing the electrical conductivity of hydrogels. The oxygen atoms of the phosphate groups in phytic acid (PA) form strong hydrogen bonds with hydroxyl (–OH) groups in the PVA molecular chains. At the same time, negatively charged phosphate groups in PA electrostatically interact with positively charged $-NH_3^+$ groups (protonated amino groups) on functionalized graphene. The "break–reorganization" of dynamic hydrogen bonds synergistically buffers stress, regulating the cyclic tensile mechanical performance of the hydrogel (Fig. 1(b)). Compared with unmodified rGO, NH_2-rGO disperses more uniformly in aqueous and PVA solutions (Figs. S1 and S2 in the Electronic Supplementary Material (ESM)). PA allows the highly efficient crosslinking through its abundant phosphate groups, while providing ion conduction sites. It also offers natural environmental friendliness and biocompatibility. This work is expected to advance the development of next-generation intelligent sign-language recognition systems, thereby improving communication for individuals with disabilities or hearing impairments (Fig. 1(c)).

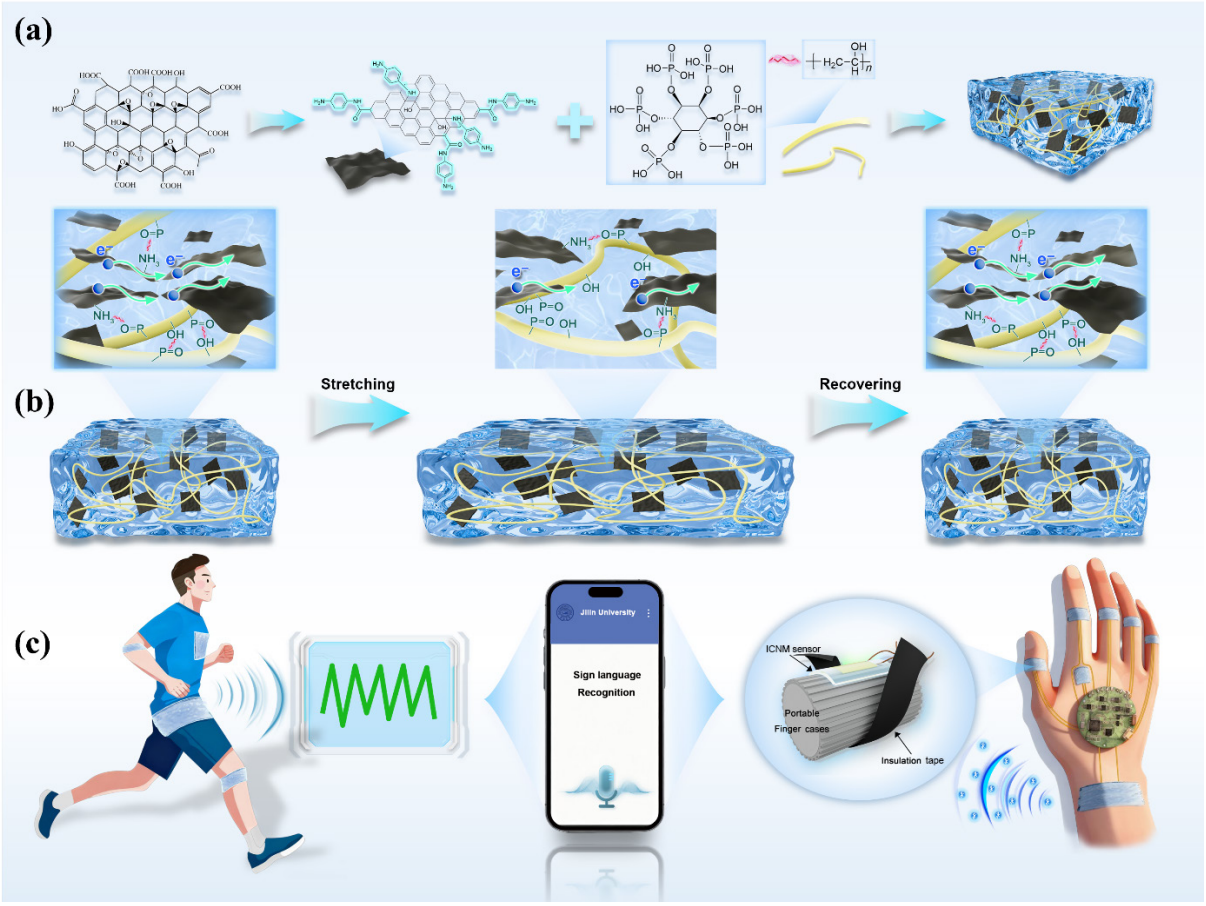

Figure 1 (a) Process diagram for the preparation of PVA/PA/NH_2-rGO hydrogel. (b) Schematic of dynamic hydrogen bonding during the tensile–recovery cycle of PVA/PA/NH_2-rGO hydrogel. (c) Application diagram of PVA/PA/NH_2-rGO hydrogel.

2 Results and discussion

2.1 Preparation of PVA/PA/NH_2-rGO hydrogels

PVA/PA/NH_2-rGO hydrogels were prepared as shown in Fig. 1(a). In the first step, the NH_2-rGO content was fixed, and the optimal proportion of PA was determined. For hydrogel preparation, 2.5 g of PVA was dissolved in 25 mL of deionized water (mass ratio of 1:10). The solution was stirred at 97 °C for 30 min until the complete dissolution of PVA, yielding a transparent solution. Subsequently, 0.1 g of NH_2-rGO was added at 97 °C and stirred for an additional hour. Different hydrogel samples were obtained through the sequential addition of various volumes of PA (2, 3, 4, 5, and 6 mL) to the aforementioned solution, followed by stirring for 1 h. The resulting precursor solutions were poured into polytetrafluoroethylene (PTFE) molds and transformed into hydrogels through multiple freeze–thaw cycles (Fig. S3 in the ESM) (freeze at −20 °C for 1 h, then thaw at room temperature (25 °C) for 30 min, repeating this cycle three times). The resulting composite hydrogels were denoted as PVA/PA_x/NH_2-$rGO_{0.1}$, where x is the PA content (x = 2, 3, 4, 5, 6).

After determining the optimal PA addition (4 mL), the effect of NH_2-rGO content on hydrogel properties was investigated. Specifically, 2.5 g of PVA was dissolved in 25 mL of deionized water (1:10 mass ratio) and stirred at 97 °C for 30 min to obtain a clear solution. Subsequently, different quantities of aqueous NH_2-rGO (0.05, 0.1, 0.15, 0.2, and 0.25 g) were added at 97 °C and stirred for 1 h. The optimal amount of PA (4 mL) was then incorporated into the aforementioned solution, the resulting solution was poured into a PTFE mold and cured via repeated freeze–thaw cycling (Fig. S3 in the ESM) (freeze at −20 °C for 1 h, then thaw at room temperature (25 °C) for 30 min, repeating this cycle three times). The obtained composite hydrogels were named PVA/PA_4/NH_2-rGO_y, where y is the NH_2-rGO content (y = 0.05, 0.1, 0.15, 0.2, 0.25). For comparison, pure PVA hydrogels without PA or NH_2-rGO were also prepared and used as control samples.

2.2 Physical and morphological characterization

Figures 2(a)–2(c) and Fig. S5 in the ESM show the morphologies and multiscale scanning electron microscopy images of the PVA, PVA/NH_2-rGO, PVA/PA, and PVA/PA_4/NH_2-$rGO_{0.1}$ hydrogels. GO exhibits a typical two-dimensional layered structure (Fig. S4(a) in the ESM). NH_2-rGO retains the lamellar structure of the original GO without agglomeration, forming a porous structure (Fig. S4(b) in the ESM). Furthermore, NH_2-rGO consists of stacked, dispersed, large, and transparent multilayer folded rGO nanosheets (Fig. S4(c) in the ESM). This indicates that the introduction of the amino group did not destroy the original structure of GO. The incorporation of amino molecular chains and the removal of oxygen-containing functional groups during reduction synergistically created discontinuous interfacial tension between lamellae, ultimately resulting in the generation of hole structures [43]. The surface and cross-sectional morphologies of the PVA hydrogel exhibit a typical three-dimensional (3D) porous network.

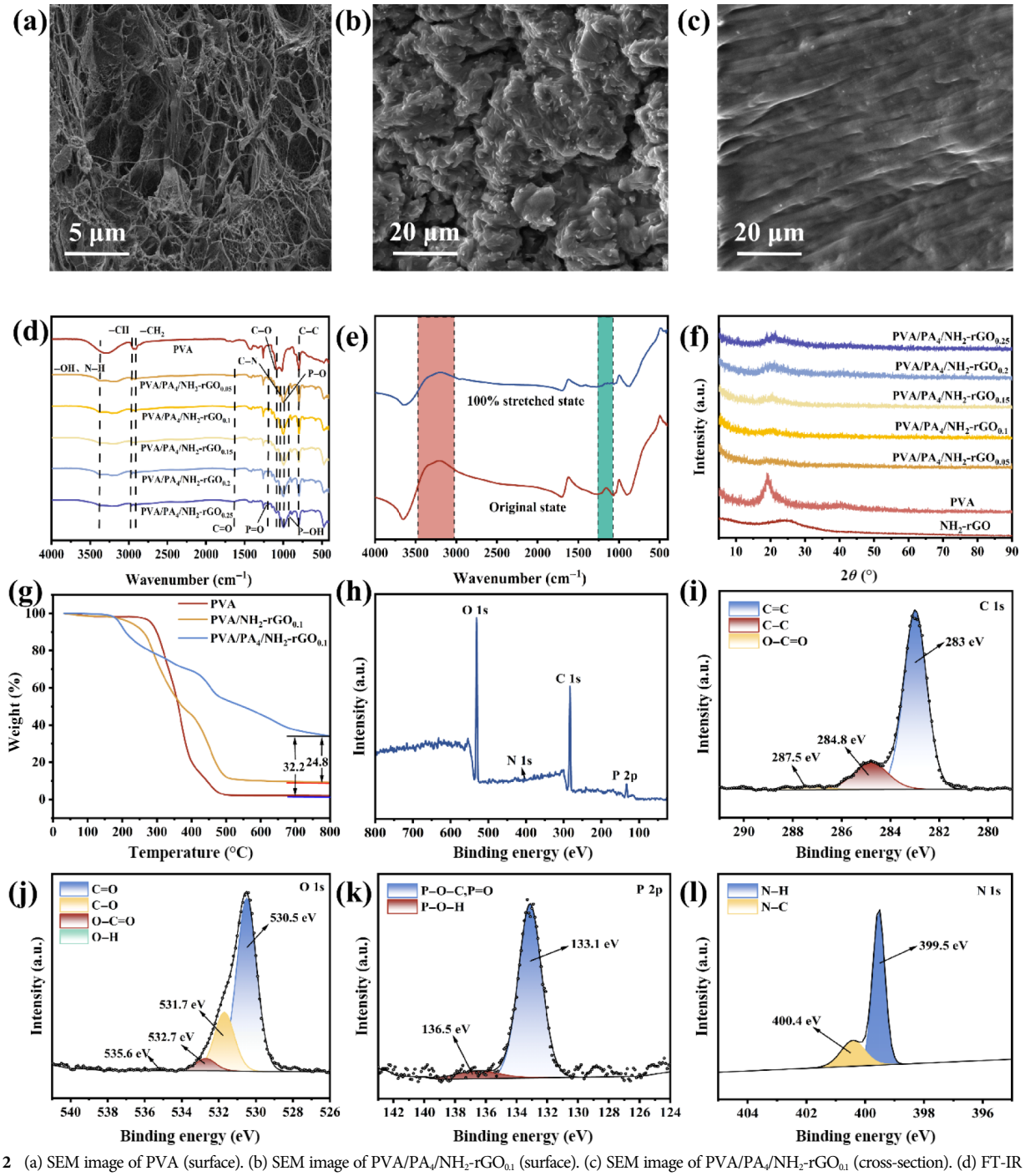

Figure 2 (a) SEM image of PVA (surface). (b) SEM image of PVA/PA_4/NH_2-$rGO_{0.1}$ (surface). (c) SEM image of PVA/PA_4/NH_2-$rGO_{0.1}$ (cross-section). (d) FT-IR spectra of PVA and different ratios of PVA/PA/NH_2-rGO hydrogels. (e) Infrared images of PVA/PA_4/NH_2-$rGO_{0.1}$ hydrogels at original length and in 100% stretched state (tested in wet state). (f) XRD spectra of NH_2-GO, PVA and different ratios of PVA/PA/NH_2-rGO hydrogels. (g) Thermogravimetric curves of PVA, PVA/NH_2-$rGO_{0.1}$, and PVA/PA_4/NH_2-$rGO_{0.1}$ hydrogel. (h) XPS full spectrum of PVA/PA_4/NH_2-$rGO_{0.1}$ hydrogel. (i)–(l) Energy spectral analyses of C 1s, O 1s, P 2p, and N 1s of PVA/PA_4/NH_2-$rGO_{0.1}$ hydrogel.

The surface pores are relatively uniformly distributed, although their sizes vary to some extent, and several interconnected pores form a honeycomb-like architecture (Fig. 2(a) and Fig. S5(a) in the ESM). The cross-section of the PVA hydrogel exhibits a more pronounced 3D porous configuration (Fig. S5(b) in the ESM) because of the use of the freeze–thaw method for curing. During the freezing stage, water in the PVA solution crystallizes into ice crystals, which occupy a certain volume within the system. Upon thawing, these ice crystals melt, leaving behind voids in the spaces they previously occupied, thereby forming a porous structure. The surface of the PVA/NH_2-rGO hydrogel also exhibits a loose porous structure, indicating that the introduction of NH_2-rGO does not disrupt the intrinsic porous network of the PVA hydrogel, preserving the original 3D structure (Fig. S5(c) in the ESM). In contrast, the PVA/PA hydrogel shows a notably denser surface with a markedly reduced number of pores (Fig. S5(d) in the ESM). This indicates that the incorporation of PA alters the surface morphology of PVA hydrogels. The polar functional groups of PA

form physically crosslinked with the hydroxyl groups of PVA, increasing the crosslink density and suppressing the formation of pores. At the same time, PVA exhibits good compatibility with PA, allowing PA molecular chains to uniformly disperse within the PVA network and fill the pores formed by the loosely arranged segments in the original PVA hydrogel. The PVA/PA_4/NH_2-$rGO_{0.1}$ hydrogel exhibits a rough and uneven surface structure and an overall denser morphology (Fig. 2(b) and Fig. S5(e) in the ESM), but its cross-section appears relatively smooth, indicating its uniform and dense internal network (Fig. 2(c) and Fig. S5(f) in the ESM). These findings indicate that PA effectively fills the internal pores in the hydrogel. During hydrogel formation, PA, NH_2-rGO sheets, and PVA chains are synergistically crosslinked, forming a composite network structure with an irregular surface. The dense structure of the PVA/PA_4/NH_2-$rGO_{0.1}$ hydrogel exhibits substantial advantages over porous systems, particularly in terms of mechanical robustness, electrical stability, and sensing performance. Collectively, these results confirm that the incorporation of PA and NH_2-rGO promotes the formation of a well-organized and crosslinked network within the PVA/PA/NH_2-rGO hydrogel.

As shown in Fig. 2(d), Fourier transform infrared (FT-IR) spectroscopy was used to investigate the compositions of the PVA/PA/NH_2-rGO hydrogels. The successful synthesis of NH_2-rGO was confirmed in our previous work [43]. The FT-IR spectrum of the PVA hydrogel shows the characteristic peaks of PVA at 2961, 2910, 1085, and 795 cm^{-1}, attributed to C–H, C–H, C–O stretching vibrations, and C–C bending vibrations, respectively. The PVA/PA/NH_2-rGO hydrogel exhibits identical characteristic peaks, with an additional peak at 3380 cm^{-1}, which was attributed to the introduction of amino groups, the formation of N–H bonds, and the combination with –OH. Moreover, the peak at 1045 cm^{-1} confirms the presence of C–N bonds. Additionally, the PVA/PA/NH_2-rGO hydrogel exhibits strong, sharp peaks at 1003 and 795 cm^{-1}, along with a weak peak at 1197 cm^{-1}. These were attributed to the stretching vibrations of P–O, bending vibrations of P–OH, and stretching vibrations of P=O, respectively, indicating the successful incorporation of NH_2-rGO and PA into the PVA hydrogel. The FT-IR spectra of PVA/PA/NH_2-rGO hydrogels with different component ratios are fundamentally consistent, with only slight shifts in peak intensities and positions. This suggests that differences in the contents of NH_2-rGO and PA do not affect the intrinsic chemical structures of the individual components. Instead, changes in the component ratios result in slight differences in the strength of intermolecular interactions, the relative content of functional groups, and the state of water. Figure 2(e) shows the FT-IR spectra of the PVA/PA_4/NH_2-$rGO_{0.1}$ hydrogel in its pristine state and under 100% tensile strain, exhibiting dynamic changes in hydrogen bonding during deformation. In the 3100–3400 cm^{-1} region, the hydrogel exhibits a broad and intense peak in the initial state, corresponding to stretching vibrations of associated hydroxyl groups. Upon 100% stretching, the intensity of the broad peak in the 3100–3400 cm^{-1} region markedly diminishes, indicating the disruption of dynamic hydrogen bonds between hydroxyl groups from PVA (–OH) and phytic acid (–PO_3H_2), and the conversion of associated hydroxyl groups into free hydroxyl groups. This observation directly confirms the "break–recombination" dynamic behavior of hydrogen bonds. In the 1000–1300 cm^{-1} region, the PVA/PA_4/NH_2-$rGO_{0.1}$ hydrogel in the original length state has a wide and strong peak, corresponding to P=O stretching vibrations of the hydrogen-bonded state. After 100% stretching, the P=O peak decreases in intensity and is blue-shifted approximately by 10–20 cm^{-1}. This shift indicates an increase in the bond force constant of P=O upon hydrogen-bond breaking and an increase in vibration frequency. These results further confirm the reversible dissociation of dynamic hydrogen bonds and validate the good cyclic performance of the PVA/PA_4/NH_2-$rGO_{0.1}$ hydrogel.

The crystal structures of NH_2-GO, PVA hydrogel, and PVA/PA/NH_2-rGO hydrogels with different component ratios were analyzed using X-ray diffraction (Fig. 2(f)). GO exhibits a sharp and intense diffraction peak at 2θ = 11.3° (Fig. S6 in the ESM). In contrast, the diffraction peaks of NH_2-GO are broader, weaker, and slightly shifted. These changes arise from hydrogen bonds and electrostatic interactions between amino groups and the oxygen-containing functional groups on GO, which shorten the interlayer distance. The reduced spacing weakens coherent X-ray scattering, resulting in diminished peak intensity and peak shifts. The PVA hydrogel shows a distinct diffraction peak at 2θ = 20°, indicating that hydroxyl groups in the molecular chains of PVA form locally ordered crystalline regions via hydrogen bonding, alongside substantial amorphous domains with randomly arranged molecular chains. However, the PVA/PA/NH_2-rGO hydrogels with different component ratios exhibit broad, low-intensity peaks near the same angle (approximately 2θ = 20°), suggesting that the introduction of PA and NH_2-rGO disrupts the native crystalline arrangement of PVA chains. The intensity of this peak gradually increases with NH_2-rGO content, which was attributed to the layered structures acting as nucleation sites, inducing the orderly arrangement of nearby parts of PVA chains via surface interactions, including hydrogen bonds between amino groups, –PO_3H_2 groups, and PVA hydroxyl groups. This slightly enhances local crystallinity, leading to a modest increase in diffraction peak intensity.

Figure 2(g) shows the thermogravimetric curves of the PVA, PVA/NH_2-$rGO_{0.1}$, and PVA/PA_4/NH_2-$rGO_{0.1}$ hydrogels in an N_2 atmosphere from room temperature to 800 °C. The thermal decomposition temperatures of the PVA and PVA/NH_2-$rGO_{0.1}$ hydrogels are nearly identical, both exhibiting pronounced and rapid decomposition above 300 °C. In contrast, the PVA/PA_4/NH_2-$rGO_{0.1}$ hydrogel starts to lose weight at approximately 200 °C and decomposes at a lower rate. Notably, the thermogravimetric curves of the three hydrogels indicate that the PVA/PA_4/NH_2-$rGO_{0.1}$ hydrogel exhibits the highest residual content after heat treatment. Its residual content is 32.2% higher than that of the PVA hydrogel and 24.8% higher than that of the PVA/NH_2-$rGO_{0.1}$ hydrogel, indicating that the incorporation of PA and NH_2-rGO enhances the char-forming ability and overall thermal stability of the composite hydrogel. The reduction in initial decomposition temperature reflects the active carbonisation behaviour of PA-catalysed PVA dehydration cross-linking, rather than a thermal stability defect. NH_2-rGO further reinforces the carbon layer through both physical barrier effects and catalytic action, ultimately forming a robust carbon skeleton that substantially enhances the material's high-temperature structural stability and carbon yield.

Figures 2(h)–2(l) show the X-ray photoelectron spectroscopy results for the PVA/PA_4/NH_2-$rGO_{0.1}$ hydrogel. Four different characteristic peaks are observed: C 1s (283.7 eV), O 1s (531.4 eV), P 2p (133.5 eV), and N 1s (399.9 eV). The N 1s peak was attributed to the binding energy of the amino group in NH_2-rGO. In the N 1s spectrum, the PVA/PA_4/NH_2-$rGO_{0.1}$ hydrogel shows notable C–N (~ 400.4 eV) and N–H (~ 399.5 eV) peaks. However, the overall

N 1s signal is relatively weak, which was attributed to the low content of NH_2-rGO in the hydrogel. The P 2p peak is attributed to the binding energy of phosphate groups in PA. In the P 2p spectrum, the PVA/PA_4/NH_2-rGO$_{0.1}$ hydrogel shows notable P–O–C, P=O (~ 133.1 eV), and P–O–H (~ 136.5 eV) peaks. Simultaneously, the characteristic peaks of functional groups unique to PVA hydrogel (e.g., C=C, C=O) are observed in the C 1s and O 1s spectra of the PVA/PA_4/NH_2-rGO$_{0.1}$ hydrogel, indicating that the functional groups of PVA retained good stability. Overall, the results of X-ray photoelectron spectroscopy confirm the successful formation of stable composite structures among PVA, PA, and NH_2-rGO.

2.3 Performance evaluation

2.3.1 Mechanical and electrical conductivity properties of PVA/PA//NH_2-rGO hydrogels

Figure 3(a) presents the compression-rebound properties of the PVA/PA_4/NH_2-rGO$_{0.1}$ hydrogel. The results indicate the good rebound of the hydrogel after compressive deformation. Even after multiple compression cycles, the hydrogel fully recovers its original shape, showing good structural stability and deformation reversibility. To further assess its mechanical performance, the hydrogel was subjected to tensile, twisting, and knotting tests.

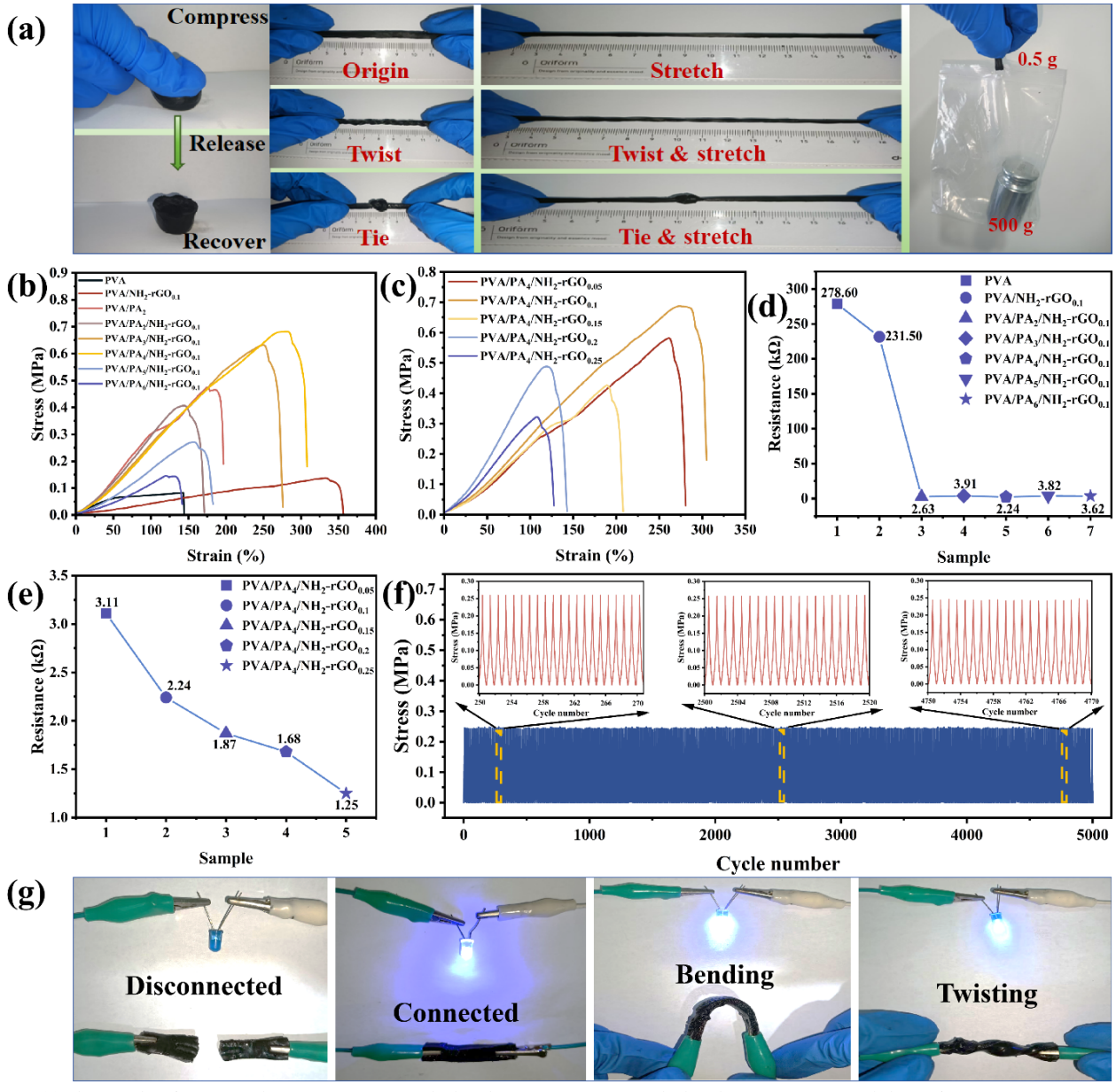

Figure 3 (a) Photographs of compressed PVA/PA_4/NH_2-rGO$_{0.1}$ hydrogel. PVA/PA_4/NH_2-rGO$_{0.1}$ hydrogel regaining its original shape after compression release. High ductility and flexibility of PVA/PA_4/NH_2-rGO$_{0.1}$ hydrogel by stretching, torsional stretching, and knotted stretching. Photograph of the PVA/PA_4/NH_2-rGO$_{0.1}$ hydrogel supporting a 500 g weight, which weighs about 1000 times the weight of the hydrogel itself. (b) Stress–strain curves of PVA hydrogel, PVA/NH_2-rGO$_{0.1}$ hydrogel, PVA/PA_2 hydrogel, and PVA/PA/NH_2-rGO hydrogel with different ratios of PA. (c) Stress–strain curves of PVA/PA/NH_2-rGO hydrogels with different ratios of NH_2-rGO. (d) Resistance change of PVA hydrogel, PVA/NH_2-rGO$_{0.1}$ hydrogel and PVA/PA/NH_2-rGO hydrogel with different ratios of PA. (e) Resistance change of PVA/PA/NH_2-rGO hydrogels with different ratios of NH_2-rGO. (f) The mechanical stability of the PVA/PA_4/NH_2-rGO$_{0.1}$ hydrogel after subjecting for 5000 cycles ofloading-unloading process (strain amplitude: 100%, room temperature 25 °C. Under constant humidity conditions: spray water every 10 min to maintain humidity). (g) Demonstration of the PVA/PA_4/NH_2-rGO$_{0.1}$ hydrogel in the flat, bending, and twisting states at −20 °C

Comparison of its length and morphology before and after these mechanical stresses reveals no observable structural damage. Moreover, load-bearing tests show that the hydrogel can support up to 1000 times its own mass without fracturing, underscoring its good mechanical strength and load-bearing capacity. Mechanistically, hydrogen bonds between the $–PO_3H_2$ groups of PA and the –OH groups of PVA partially break under stretching, which buffers the applied stress. These bonds are preferentially reformed upon the removal of force, driving the initial recovery of the network. Strong electrostatic interactions between the $–PO_3^-$ groups of PA and the $–NH_3^+$ groups of NH_2-rGO, characterized by high bond energy, remain largely intact during deformation, acting as "rigid support points" that stabilize the network and prevent its collapse. This dynamic "break–reorganization" of hydrogen bonds substantially enhances the mechanical cycling performance of the PVA/PA/NH_2-rGO composite hydrogel. Comparison of the tensile properties of PVA/PA_4/NH_2-$rGO_{0.1}$ hydrogels with those of pure PVA hydrogels reveals that the addition of appropriate amounts of NH_2-rGO and PA substantially improves the tensile strength of PVA hydrogels. Among samples with different NH_2-rGO and PA contents, the PVA/PA_4/NH_2-$rGO_{0.1}$ hydrogel exhibits optimal mechanical properties, showing a tensile strength of 0.7 MPa and an elongation at break of 305%, thus striking a favorable balance between strength and ductility (Figs. 3(b) and 3(c)). In contrast, excessive contents of NH_2-rGO and PA adversely affect mechanical performance. This was attributed to the agglomeration tendency driven by intermolecular forces (hydrogen bonding and π–π stacking) when NH_2-rGO is present in excess, causing stress concentration that makes the hydrogel prone to fracture. Furthermore, an overly high crosslinking density induced by the excess of NH_2-rGO and PA restricts molecular chain movement, rendering the hydrogel rigid and more susceptible to fracture.

The incorporation of small amounts of NH_2-rGO and PA markedly decreases the electrical resistance of PVA/PA/NH_2-rGO hydrogels (Figs. 3(d) and 3(e)). The PVA/PA_4/NH_2-$rGO_{0.1}$ hydrogel exhibits a conductivity of 1.1 S/m at room temperature and 0.0704 S/m at −20 °C. We tested the electrical conductivity under different temperature/humidity conditions, as shown in Table S1 in the ESM. NH_2-rGO, serving as an electron-type conductive filler, possesses high intrinsic conductivity, enabling efficient electron transfer via π–π interactions between graphene layers or through direct contact, thereby establishing stable electron conduction pathways within the hydrogel. Concurrently, PA, an organic molecule containing polyphosphate groups ($–PO_4H_2$), readily dissociates in the aqueous environment of the hydrogel, generating abundant ions, such as H^+, $H_2PO_4^-$, and HPO_4^{2-}. This increases the concentration of ionic charge carriers within the hydrogel, optimizes the ionic conduction environment, and further reduces the electrical resistance of the hydrogel. The combined effect of electronic conduction through NH_2-rGO and ionic conduction via PA constitutes a "dual-conduction mechanism", which substantially increases the overall conductivity of the PVA/PA_4/NH_2-$rGO_{0.1}$ hydrogel.

The cyclic performance of the PVA/PA_4/NH_2-$rGO_{0.1}$ hydrogel under constant-humidity tensile loading (Fig. 3(f)) and at room temperature (Fig. S7 in the ESM) was also evaluated. After 5000 loading–unloading cycles at 100% strain, the hydrogel retains good fatigue resistance and long-term stability, indicating its good mechanical properties. At low temperatures, the PVA/PA_4/NH_2-$rGO_{0.1}$ hydrogel can readily illuminate an external light-emitting diode (LED) when connected to an external power source, with brightness remaining stable under arbitrary bending and twisting (Fig. 3(g)). Furthermore, the PVA/PA_4/NH_2-$rGO_{0.1}$ hydrogel maintains nearly pristine mechanical properties at −20 °C (Figs. S8(a) and S8(b) in the ESM) and exhibits high flexibility, allowing arbitrary bending. In contrast, the pure PVA hydrogel becomes rigid and brittle under the same low-temperature conditions, fracturing during bending (Figs. S8(c) and S8(d) in the ESM). To further evaluate the low-temperature conductivity of the PVA and PVA/PA_4/NH_2-$rGO_{0.1}$ hydrogels, they were subjected to LED conductivity tests at −20 °C (placed at −20 °C for 24 h) and 20 °C. As shown in Figs. S8(e) and S8(f) in the ESM, the PVA hydrogel exhibits negligible conductivity at −20 °C, whereas the PVA/PA_4/NH_2-$rGO_{0.1}$ hydrogel maintains good conductivity. Even at 20 °C, the PVA hydrogel shows weaker conductivity than the PVA/PA_4/NH_2-$rGO_{0.1}$ hydrogel. These results indicate the good freeze resistance of the PVA/PA_4/NH_2-$rGO_{0.1}$ hydrogel. This behavior was attributed to dense hydrogen-bond networks formed between the phosphate groups in PA, hydroxyl groups in PVA, and water molecules within the hydrogel, which trap free water, suppress the nucleation and growth of ice crystals at low temperatures, and stabilize the overall hydrogel network, ultimately conferring good freeze resistance to the PVA/PA/NH_2-rGO hydrogel. In summary, the PVA/PA_4/NH_2-$rGO_{0.1}$ hydrogel exhibits good mechanical strength, ionic conductivity, and freeze resistance, highlighting its potential for robust low-temperature and flexible electronic applications.

2.3.2 *Sensing performance of the PVA/PA/NH_2-rGO hydrogels*

The application of hydrogels in flexible sensing was investigated by observing changes in relative resistance and relative capacitance at the same and different strains (Fig. 4). Samples were mounted on a tensile testing machine and connected to a bridge tester to record electrical signals. The sensitivity of the hydrogels was evaluated using the sensitivity factor (gauge factor (GF)), which was calculated from the slope of relative resistance change ($\Delta R/R_0$) and relative capacitance ($\Delta C/C_0$) versus strain (Eqs. (S1)–(S4) in the ESM). The PVA/PA/NH_2-rGO hydrogel exhibits dual sensing responses. Movies S1 and S2 in the ESM show the relative electronic change and relative capacitance change produced by the PVA/PA_4/NH_2-$rGO_{0.1}$ hydrogel with finger bending. Hydrogel deformation alters its conductive network and dielectric constant, thereby enabling resistive and capacitive sensing responses. With increasing tensile strain, $\Delta R/R_0$ increases while $\Delta C/C_0$ decreases (Figs. 4(a) and 4(b)). Within the small strain (8%) and large strain (268%) ranges, the relative resistance and relative capacitance exhibit substantial changes, and the GF is large. This was attributed to the change in hydrogel morphology during stretching, which increases the length of conductive pathways, thereby raising the relative resistance. Simultaneously, under tensile strain, the expansion of the NH_2-rGO conductive network increases interlayer spacing and causes the partial "breakage" of electronic pathways, leading to a sharp rise in resistance. When rebound occurs after force unloading, the lamellar spacing decreases and new electronic contact points are added, considerably reducing resistance. This "dramatic change in pathway" directly amplifies the signal amplitude and improves sensitivity. Furthermore, the dielectric constant of the composite decreases during stretching, and the contracted double-layer interface results in diminished capacitance. The GF of the hydrogel can be divided into four linear response

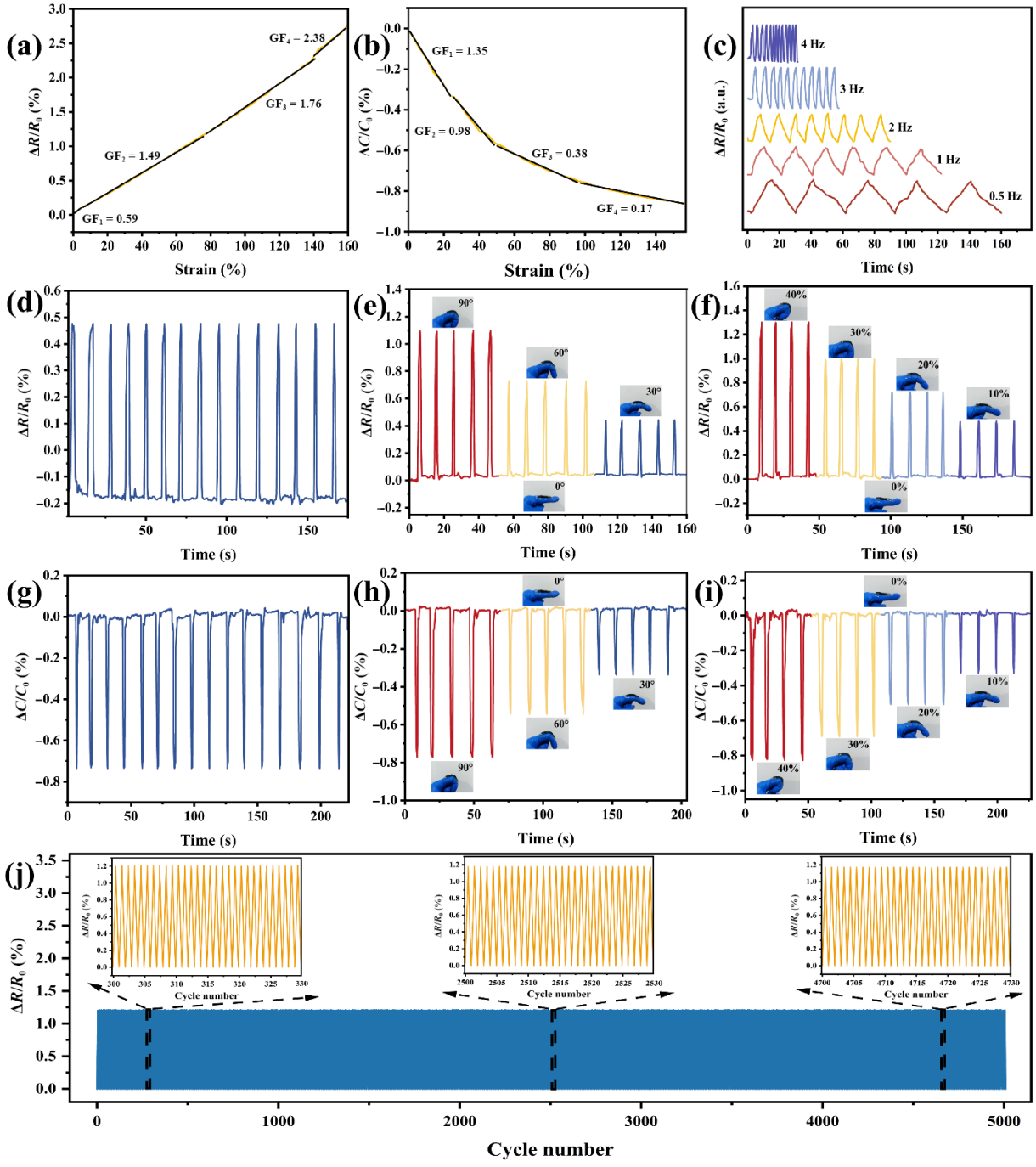

Figure 4 Characterisation of the sensing performance of PVA/PA_4/NH_2-$rGO_{0.1}$ hydrogel. (a) and (b) Relative resistance and capacitance changes as well as tension sensitivity GF of PVA/PA_4/NH_2-$rGO_{0.1}$ hydrogel at different strains. (c) Relative resistance changes of the hydrogel sensor during 100% stretching at different frequencies. (d) Relative resistance changes of PVA/PA_4/NH_2-$rGO_{0.1}$ hydrogel at the same strain. (e) Relative resistance changes of PVA/PA_4/NH_2-$rGO_{0.1}$ hydrogel at 0°, 30°, 60°, and 90° of finger bending. (f) Relative resistance changes of PVA/PA_4/NH_2-$rGO_{0.1}$ hydrogel at 0%, 10%, 20%, 30%, and 40% of strain. (g) Relative capacitance changes of PVA/PA_4/NH_2-$rGO_{0.1}$ hydrogel at the same strain. (h) Relative capacitance changes of PVA/PA_4/NH_2-$rGO_{0.1}$ hydrogel at 0°, 30°, 60°, and 90° of finger bending. (i) Relative capacitance changes of PVA/PA_4/NH_2-$rGO_{0.1}$ hydrogel at 0%, 10%, 20%, 30%, and 40% of strain. (j) The relative resistance changes of the PVA/PA_4/NH_2-$rGO_{0.1}$ hydrogel upon 100% strain for 5000 cycles without any resting (room temperature 25 °C; under constant humidity conditions: spray water every 10 min to maintain humidity).

regions, indicating that the PVA/PA/NH_2-rGO hydrogel exhibits high strain sensitivity in a broad strain range. Additionally, the PVA/PA_4/NH_2-$rGO_{0.1}$ hydrogel sensor exhibits stable and repeatable changes in resistance at different stretch–recovery frequencies under 100% strain. The nearly identical amplitudes of relative resistance change across various stretching rates, along with clear periodicity even under short loading–unloading cycles, indicate the high sensitivity and signal stability of the PVA/PA/NH_2-rGO hydrogel sensor (Fig. 4(c)).

The PVA/PA_4/NH_2-$rGO_{0.1}$ hydrogel exhibits rapid response (330 ms) and recovery (330 ms), suggesting its good responsiveness (Fig. S9 in the ESM). During cyclic stretch–release tests, the PVA/PA_4/NH_2-$rGO_{0.1}$ hydrogel maintains highly stable and reliable electrical signals, with both the relative resistance and relative

capacitance remaining nearly unchanged under identical strain conditions (Figs. 4(d) and 4(g)). When the strain returned to its initial state, the electrical signals correspondingly recovered to their original levels, indicating the strong elastic resilience of the material. In addition, the hydrogel effectively detected finger bending at angles of 30°, 60°, and 90°, generating distinguishable electrical signals through substantial changes in relative resistance and relative capacitance (Figs. 4(e), 4(f), 4(h), and 4(i)). These results confirm its capability for the real-time monitoring of human motions and the detection of physiological signals. Long-term stability is a critical metric for flexible sensors applied in smart wearable sensing devices. To evaluate the stability of the PVA/PA_4/NH_2-$rGO_{0.1}$ hydrogel, cyclic strain sensing tests were performed under constant humidity (Fig. 4(j)) and at room temperature (Fig. S10 in the ESM) at 100% strain. The electrical signals exhibit no notable attenuation after 5000 cycles, indicating good cycling durability. Collectively, the hydrogel integrates rapid responsiveness, high sensitivity, good repeatability, and long-term operational stability, showing promise for practical applications in flexible sensing devices.

To comprehensively assess the reliability of the signal output from the PVA/PA_4/NH_2-$rGO_{0.1}$ hydrogel, it was affixed to different parts of the human body, and its response characteristics to both minute strains and large movements were tested (Fig. 5). In microstrain monitoring scenarios, the hydrogel exhibited good sensitivity and signal stability. It accurately converted subtle, low-amplitude deformations—such as subtle facial skin contractions during breathing or frowning, slight neck muscle tension during swallowing, and gentle pressure—into electrical signals with clear and distinguishable waveforms (Figs. 5(b)–5(d) and 5(h)). These results confirm its suitability for the high-precision monitoring of micro-physiological human activities. The hydrogel also showed good dynamic response in large-strain scenarios. During movements involving large displacement, such as wrist flexion, wrist rotation, elbow flexion, and knee flexion, the PVA/PA_4/NH_2-$rGO_{0.1}$ hydrogel reliably captured changes in electrical signals with good dynamic response rates and movement synchronization (Figs. 5(e)–5(g) and 5(i)). This demonstrates its ability to effectively distinguish between different types of large-amplitude movement signals, highlighting its practical value for the real-time monitoring of human motion states. To further validate the ability of the PVA/PA_4/NH_2-$rGO_{0.1}$ hydrogel to recognize and convert complex physical stimuli into electrical signals, two characteristic deformations of short and long lines were generated by controlling the hydrogel, successfully encoding words "HYDROGEL", "SENSOR", and "GESTURE" in the Morse code (Figs. 5(j)–5(l)). Test results indicate the remarkable regularity and clarity of electrical signals during encoding, proving that this hydrogel can stably convert complex physical stimuli into interpretable electrical signals. The successful implementation of Morse code simulation further highlights its application potential in information transmission and complex signal recognition, providing critical performance support for its expanded use in flexible electronic devices, smart wearables, and other fields.

2.3.3 *PVA/PA/NH_2-rGO hydrogel applications*

In addition to their primary application in human motion monitoring, an intelligent sign language recognition system was developed using the PVA/PA/NH_2-rGO hydrogel sensors. Considering that sign language heavily relies on hand movement, multiple sensors were mounted on the interphalangeal joints of each finger, to collect abundant data during hand movement and increase the accuracy of sign language recognition (Fig. 6(a)). Movie S3 in the ESM shows the recognition of different gestures converted into pictures and text. Furthermore, the signal processing and wireless transmission systems were integrated into a printed circuit board to construct a complete system (Figs. S11(a) and S11(b) in the ESM). Once the first-hand resistive signals during hand movement were acquired, the processing system converted them into digital signals using a multichannel resistance acquisition circuit, followed by wireless transmission to the mobile application for gesture recognition (Fig. 6(a)). Compared with other multicomponent hydrogels, the PVA/PA/NH_2-rGO hydrogel shows comprehensive advantages in mechanical properties, electrical conductivity, antifreezing capability, and sensing performance. These features provide reliable material support for the design, fabrication, and performance optimization of wearable sensor components (Fig. 6(b)) [44–51]. During the gesture transition from "1" to "10," the thumb, index finger, middle finger, ring finger, and little finger bend accordingly. Correspondingly, the stretching deformation of each hydrogel sensor induces distinct changes in the electrical signals of their respective sensing channels, enabling the accurate identification of different numerical gestures (Fig. 6(c)). More importantly, the intelligent sign language recognition system is capable of converting recognized gestures into text and image outputs displayed on a mobile device. As a proof of concept, the mobile application successfully identified five representative gestures—"OK", "Good", "Hello", "Hydrogel", and "Composite materials"—with high sensitivity and accuracy (Fig. 6(d)). The regression algorithm results indicate that the sensor achieved verification accuracy rates of 98.6% and 97.3% for recognising ten digits and five words, respectively. The confusion matrix from classifier testing is shown in Figs. S12(a) and S12(b) in the ESM. This demonstrates that sign language translation using combined gestures exhibits exceptionally high classification accuracy. These results clearly highlight the superior performance and promising application potential of PVA/PA/NH_2-rGO hydrogels in wearable sensing systems and intelligent human–machine interaction technologies.

3 Conclusions

NH_2-rGO, as a functionalized graphene derivative, is non-toxic and environmentally friendly, while PA exhibits excellent environmental sustainability and biocompatibility. Both materials meet the requirements for green and bio-friendly applications. NH_2-rGO and PA were employed to prepare a PVA/PA/NH_2-rGO composite conductive hydrogel. Experimental results show the better comprehensive performance of this composite hydrogel compared with the pristine PVA hydrogel. Specifically, the PVA/PA_4/NH_2-$rGO_{0.1}$ hydrogel exhibited a tensile strength of 0.7 MPa and an elongation at break of 305%. NH_2-rGO, serving as a conductive filler, works in conjunction with PA to improve the electrical conductivity and sensing performance of the hydrogel. Moreover, the PVA/PA/NH_2-rGO hydrogel was successfully operated as a flexible wearable strain sensor for gesture recognition. With the assistance of machine learning algorithms, a stable and reliable sign language translation system was developed, enabling the highly precise recognition of various representative sign language gestures. This work broadens the practical application

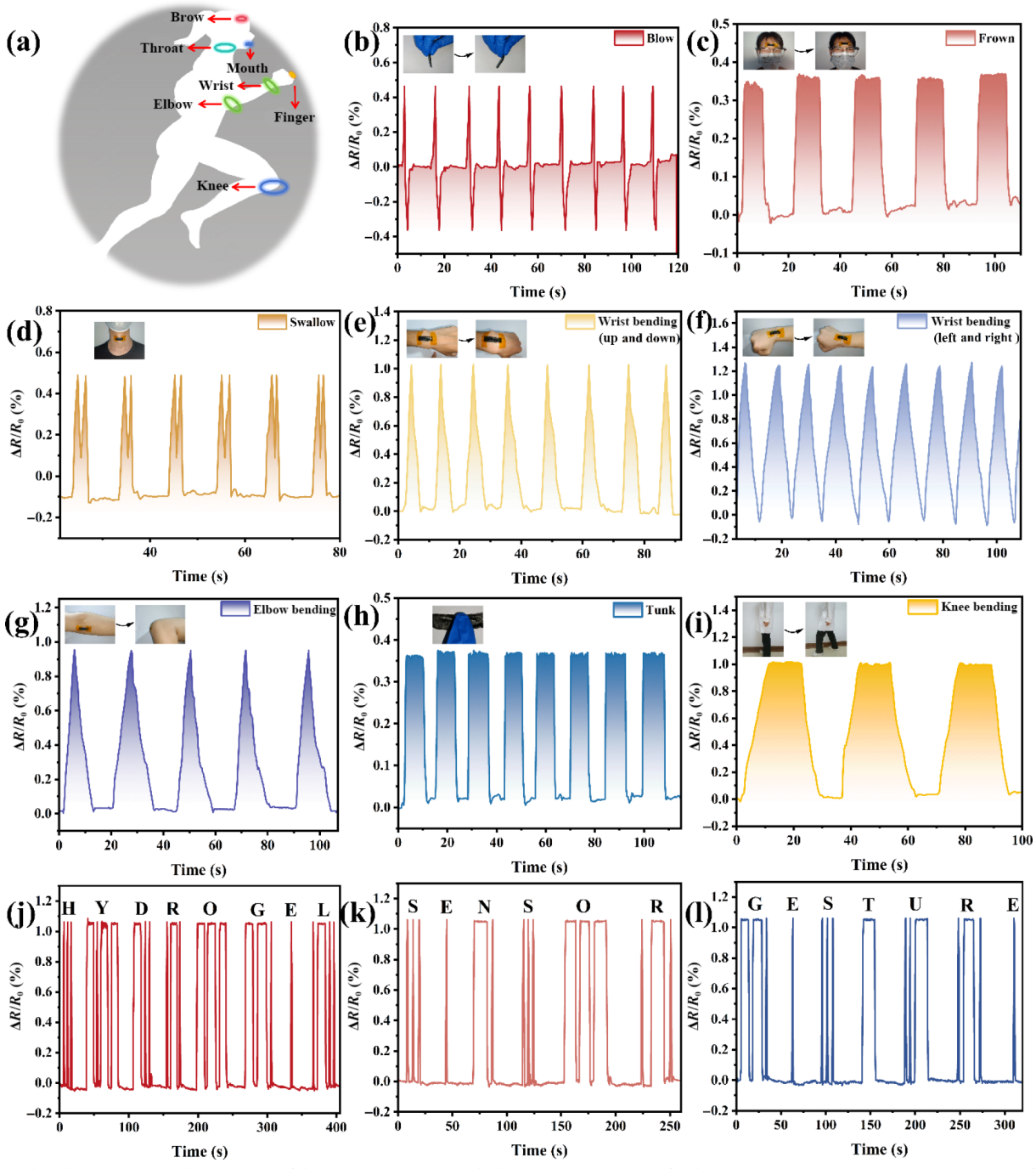

Figure 5 The relative resistance change curves of the PVA/PA_4/NH_2-$rGO_{0.1}$ hydrogel as a strain sensor for detecting various human motions. (a) Diagram of human body parts. (b) Variation in relative resistance of the PVA/PA_4/NH_2-$rGO_{0.1}$ hydrogel during human breath detection. (c) Variation in relative resistance during eyebrow furrowing. (d) Variation in relative resistance during swallowing of saliva. (e) Variation in relative resistance during wrist bending. (f) Variation in relative resistance during wrist rotation. (g) Variation in relative resistance during elbow flexion. (h) Variation in relative resistance during pressed by a finger. (i) Variation in relative resistance during knee flexion. (j)–(l) "HYDROGEL", "SENSOR", and "GESTURE" in Morse code generated through finger tapping.

prospects of PVA/PA/NH_2-rGO hydrogels in cutting-edge fields such as human–machine interfaces, smart wearable devices, and the Internet of Things. It further highlights the research value and application potential of this hydrogel in flexible electronics and intelligent sensing.

Electronic Supplementary Material: Supplementary material (additional experimental details and photos of experimental results, including preparation of graphene oxide, preparation of amino-functionalized redox graphene, test methods for strain sensors, sensing sensitivity equation, XRD patterns, etc.) is available in the online version of this article at https://doi.org/10.26599/NR.2026.94908664.

Data availability

All data needed to support the conclusions in the paper are presented in the manuscript and the Electronic Supplementary

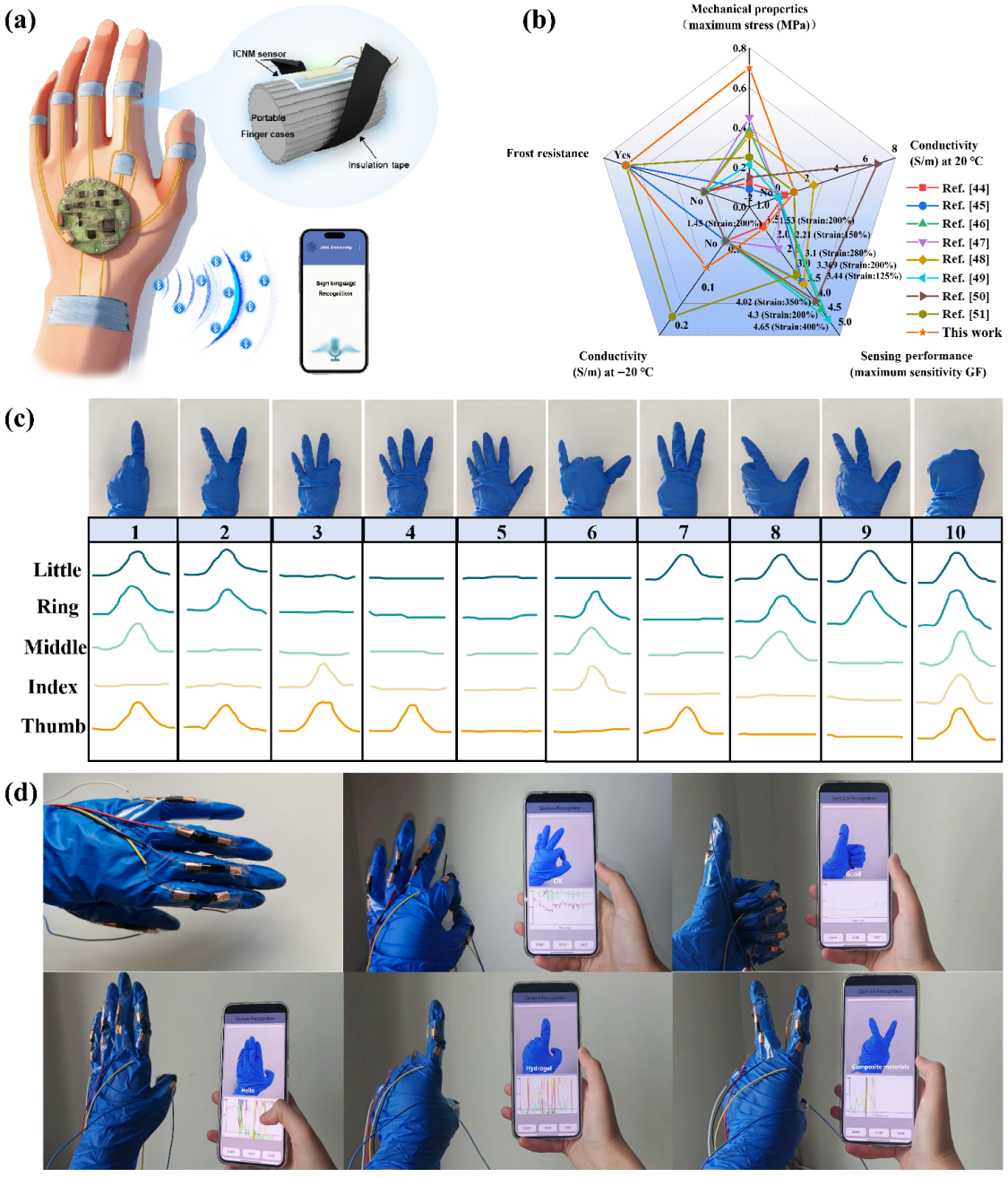

Figure 6 (a) Schematic diagram of the sign language recognition system for converting sign language to text. (b) Radargram comparing the multifunctional properties of PVA/PA_4/NH_2-$rGO_{0.1}$ hydrogel with those of various materials. (c) The ten digits (1–10) of the gesture correspond to the generated resistance change curve. (d) An intelligent sign language recognition system translates the gestures for five words into text and displays them in real-time on the mobile application interface with photographs.

Material. Additional data related to this paper may be requested from the corresponding author upon request.

Acknowledgements

This study was supported by the Natural Science Foundation of Inner Mongolia (Nos. 2024LHMS05043 and 2025LHMS05038).

Declaration of competing interest

The authors declare that they have no known competing financial interests or personal relationships that could have appeared to influence the work reported in this paper.

Author contribution statement

K. Q. Z.: Writing – original draft, performed experiments, methodology, investigation, formal analysis, conceptualization. T. T. Y. and D. Z.: Investigation, performed figure preparation. R. G. X. and Y. N. L.: Review & editing, supervision, methodology, conceptualization. L. N. J. and H. T. Y.: Review & editing, supervision. All authors have approved the final manuscript.

Use of AI statement

None.

References

[1] Geng, S. Y.; Fan, S. Q.; Li, H. F.; Qi, Y. S.; An, C. H.; Wu, E. X.; Su, J.; Liu, J. An artificial neuromuscular system for bimodal human-machine interaction. *Adv. Funct. Mater.* **2023**, *33*, 2302345.

[2] Liu, W. B.; Duo, Y. N.; Chen, X. Y.; Chen, B. H.; Bu, T. Z.; Li, L.; Duan, J. X.; Zuo, Z. H.; Wang, Y.; Fang, B. et al. An intelligent robotic system capable of sensing and describing objects based on bimodal, self-powered flexible sensors. *Adv. Funct. Mater.* **2023**, *33*, 2306368.

[3] Ding, Y. C.; Jiang, J. X.; Wu, Y. S.; Zhang, Y. K.; Zhou, J. H.; Zhang, Y. F.; Huang, Q. Y.; Zheng, Z. J. Porous conductive textiles for wearable electronics. *Chem. Rev.* **2024**, *124*, 1535–1648.

[4] Yao, K.; Ling, Y.; Yang, J. J.; Pan, Z. H.; Xing, R. G.; Zhang, Q. C. Cobalt-doping unlocks copper self-healing chemistry in copper hexacyanoferrate for long-cycling aqueous Mg-ion storage. *J. Am. Chem. Soc.* **2026**, *148*, 8686–8699.

[5] Li, T.; Qi, H. B.; Dong, X. Y.; Li, G. J.; Zhai, W. Highly robust conductive organo-hydrogels with powerful sensing capabilities under large mechanical stress. *Adv. Mater.* **2024**, *36*, 2304145.

[6] Liu, R. N.; Liu, Y. Y.; Fu, S. M.; Cheng, Y. G.; Jin, K. M.; Ma, J. T.; Wan, Y. C.; Tian, Y. Humidity adaptive antifreeze hydrogel sensor for intelligent control and human-computer interaction. *Small* **2024**, *20*, 2308092.

[7] Liu, R. J.; Wang, T. J.; Li, G. F.; Fan, Z. Y.; Zhou, Q.; Wang, K.; Li, P.; Huang, W. Self-reinforced hydrogel-based skin-contactable flexible electronics for multimodal electrophysiological signal monitoring and emergency alarming system. *Adv. Funct. Mater.* **2023**, *33*, 2214917.

[8] Wang, Z. Y.; Bu, M. M.; Xiu, K. H.; Sun, J. Y.; Hu, N.; Zhao, L. B.; Gao, L. X.; Kong, F. Z.; Zhu, H.; Song, J. et al. A flexible, stretchable and triboelectric smart sensor based on graphene oxide and polyacrylamide hydrogel for high precision gait recognition in Parkinsonian and hemiplegic patients. *Nano Energy* **2022**, *104*, 107978.

[9] Roy, A.; Manna, K.; Ray, P. G.; Dhara, S.; Pal, S. β-Cyclodextrin-based ultrahigh stretchable, flexible, electro- and pressure-responsive, adhesive, transparent hydrogel as motion sensor. *ACS Appl. Mater. Interfaces* **2022**, *14*, 17065–17080.

[10] Liu, R. N.; Liu, Y. Y.; Cheng, Y. G.; Liu, H.; Fu, S. M.; Jin, K. M.; Li, D. L.; Fu, Z. W.; Han, Y. X.; Wang, Y. P. et al. Aloe inspired special structure hydrogel pressure sensor for real-time human-computer interaction and muscle rehabilitation system. *Adv. Funct. Mater.* **2023**, *33*, 2308175.

[11] Xu, X. H.; Gao, F. L.; Tian, L.; Yang, Z. Y.; Yu, Z. Z.; Shang, J.; Li, R. W.; Li, X. F. Ultra-sensitive and high-resolution flexible thermoelectric sensor enabled by p-n heterojunction array structure. *Matter* **2025**, *8*, 102265.

[12] Tian, L.; Gao, F. L.; Li, Y. X.; Yang, Z. Y.; Xu, X. H.; Yu, Z. Z.; Shang, J.; Li, R. W.; Li, X. F. High-performance bimodal temperature/pressure tactile sensor based on lamellar CNT/MXene/Cellulose nanofibers aerogel with enhanced multifunctionality. *Adv. Funct. Mater.* **2025**, *35*, 2418988.

[13] Gao, F. L.; Liu, J.; Li, X. P.; Ma, Q.; Zhang, T. T.; Yu, Z. Z.; Shang, J.; Li, R. W.; Li, X. F. $Ti_3C_2T_x$ MXene-based multifunctional tactile sensors for precisely detecting and distinguishing temperature and pressure stimuli. *ACS Nano* **2023**, *17*, 16036–16047.

[14] Wen, F.; Zhang, Z. X.; He, T. Y. Y.; Lee, C. AI enabled sign language recognition and VR space bidirectional communication using triboelectric smart glove. *Nat. Commun.* **2021**, *12*, 5378.

[15] Zhu, M. L.; Sun, Z. D.; Lee, C. Soft modular glove with multimodal sensing and augmented haptic feedback enabled by materials' multifunctionalities. *ACS Nano* **2022**, *16*, 14097–14110.

[16] Pyun, K. R.; Kwon, K.; Yoo, M. J.; Kim, K. K.; Gong, D.; Yeo, W. H.; Han, S.; Ko, S. H. Machine-learned wearable sensors for real-time hand-motion recognition: Toward practical applications. *Natl. Sci. Rev.* **2024**, *11*, nwad298.

[17] Guo, Z. H.; Wang, H. L.; Shao, J. J.; Shao, Y. S.; Jia, L. Y.; Li, L. W.; Pu, X.; Wang, Z. L. Bioinspired soft electroreceptors for artificial precontact somatosensation. *Sci. Adv.* **2022**, *8*, eabo5201.

[18] Xiang, Z. Y.; Li, L. H.; Lu, Z. H.; Yu, X. X.; Cao, Y. W.; Tahir, M.; Yao, Z. Y.; Song, Y. L. High-performance microcone-array flexible piezoelectric acoustic sensor based on multicomponent lead-free perovskite rods. *Matter* **2023**, *6*, 554–569.

[19] Su, T. Y.; Yang, J. Y.; Yu, H. T.; Xing, R. G.; Ge, X.; Jia, L. N.; Wang, Y. F.; Bao, J. X.; Pan, G. F.; Feng, W. Multiresponsive and mechanically robust self-healing waterborne polyurethane with photoluminescent and acid-base adaptive properties. *Macromolecules* **2025**, *58*, 12643–12655.

[20] Zhao, L. J.; Xu, H.; Liu, L. C.; Zheng, Y. Q.; Han, W.; Wang, L. L. MXene-induced flexible, water-retention, semi-interpenetrating network hydrogel for ultra-stable strain sensors with real-time gesture recognition. *Adv. Sci.* **2023**, *10*, 2303922.

[21] Song, B.; Dai, X. D.; Fan, X.; Gu, H. B. Wearable multifunctional organohydrogel-based electronic skin for sign language recognition under complex environments. *J. Mater. Sci. Technol.* **2024**, *181*, 91–103.

[22] Li, W.; Wu, S. X.; Li, S. M.; Zhong, X. Y.; Zhang, X. B.; Qiao, H.; Kang, M. C.; Chen, J. H.; Wang, P.; Tao, L. Q. Gesture recognition system using reduced graphene oxide-enhanced hydrogel strain sensors for rehabilitation training. *ACS Appl. Mater. Interfaces* **2023**, *15*, 45106–45115.

[23] Chen, K.; Liu, B. Y.; Hu, N.; Fan, Q. L.; Zhan, F. W.; Zhang, Z.; Ni, Z. H.; Li, X.; Hu, T. A biodegradable, highly sensitive and multifunctional mechanical sensor based on rGO-silk fibroin hydrogel for human motion detection and gesture recognition. *J. Mater. Chem. A* **2024**, *12*, 3283–3293.

[24] Zhou, H. W.; Wang, Z. W.; Zhao, W. F.; Tong, X. M.; Jin, X. L.; Zhang, X. C.; Yu, Y.; Liu, H. B.; Ma, Y. C.; Li, S. S. et al. Robust and sensitive pressure/strain sensors from solution processable composite hydrogels enhanced by hollow-structured conducting polymers. *Chem. Eng. J.* **2021**, *403*, 126307.

[25] Hu, F. H.; Yu, D. H.; Dong, B. T.; Gong, X.; Li, Z. Y.; Zhao, R.; Wang, Q.; Li, G. D.; Wang, H. L.; Liu, W. X. et al. Antibacterial conductive hydrogels with freeze-directed microstructures reinforced by polyaniline-encapsulated bacterial cellulose for flexible sensors. *Chem. Eng. J.* **2025**, *512*, 162702.

[26] He, X. F.; Zeng, Z. F.; Ni, Q. Y.; Xu, Z. C.; Mao, P. F.; Jiang, B. Y.; Wu, Q.; Wang, B.; Gong, L. X.; Tang, L. C. et al. Mechanical robust and highly conductive composite hydrogel reinforced by a combination of cellulose nanofibrils/polypyrrole toward high-performance strain sensor. *Compos. Part B: Eng.* **2023**, *266*, 111022.

[27] Liu, X. L.; Shi, H. Y.; Song, F. F.; Yang, W. H.; Yang, B. W.; Ding, D. Y.; Liu, Z.; Hui, L. F.; Zhang, F. S. A highly sensitive and anti-freezing conductive strain sensor based on polypyrrole/cellulose nanofiber crosslinked polyvinyl alcohol hydrogel for human motion detection. *Int. J. Biol. Macromol.* **2024**, *257*, 128800.

[28] Huang, W. X.; Ding, Q. L.; Wang, H.; Wu, Z. X.; Luo, Y. B.; Shi, W. X.; Yang, L.; Liang, Y. J.; Liu, C.; Wu, J. Design of stretchable and self-powered sensing device for portable and remote trace biomarkers detection. *Nat. Commun.* **2023**, *14*, 5221.

[29] Wang, L.; Zhang, M. Y.; Yang, B.; Ding, X. Y.; Tan, J. J.; Song, S. X.; Nie, J. Y. Flexible, robust, and durable aramid fiber/CNT composite paper as a multifunctional sensor for wearable applications. *ACS Appl. Mater. Interfaces* **2021**, *13*, 5486–5497.

[30] Sun, M. M.; Li, P. Y.; Qin, H. Y.; Liu, N.; Ma, H. D.; Zhang, Z. L.;

Li, J. Y.; Lu, B. Y.; Pan, X. F.; Wu, L. D. Liquid metal/CNTs hydrogel-based transparent strain sensor for wireless health monitoring of aquatic animals. *Chem. Eng. J.* **2023**, *454*, 140459.

[31] Lu, Y. Y.; Yang, G.; Wang, S. Q.; Zhang, Y. Q.; Jian, Y. H.; He, L.; Yu, T.; Luo, H. Y.; Kong, D. P.; Xianyu, Y. L. et al. Stretchable graphene-hydrogel interfaces for wearable and implantable bioelectronics. *Nat. Electron.* **2024**, *7*, 51–65.

[32] Zheng, Z. J.; Xu, W. J.; Wang, Y.; Xiong, W. J.; Xiong, C. H.; You, L. J.; Wang, S. Y. High-conductivity and long-term stability strain sensor based on silk fibroin and polyvinyl alcohol hydrogels. *Mater. Today Commun.* **2024**, *38*, 108465.

[33] Shi, X. L.; Fan, X. Q.; Zhu, Y. B.; Liu, Y.; Wu, P. Q.; Jiang, R. H.; Wu, B.; Wu, H. A.; Zheng, H.; Wang, J. B. et al. Pushing detectability and sensitivity for subtle force to new limits with shrinkable nanochannel structured aerogel. *Nat. Commun.* **2022**, *13*, 1119.

[34] Chen, X. H.; Wang, Y. M.; Wang, A.; Xu, L.; Du, B. Y.; Guo, D. L.; Zhao, H. F.; Sha, L. Z. Demethylated lignin-reinforced multifunctional polyvinyl alcohol-based composites materials enabled by natural physical intertwining effect. *Chem. Eng. J.* **2025**, *509*, 161192.

[35] Zhang, Z. W.; Zhang, W. J.; Ding, L.; Liu, M.; Zheng, B. W.; Yi, C. X.; Chen, J.; Zhou, S. Soft-tough polyacrylamide and polyacrylamide/polyvinyl alcohol/sodium alginate bilayer hydrogels for adaptive grasping and shape recognition. *Carbohydr. Polym.* **2025**, *367*, 123973.

[36] Ieamviteevanich, P.; Palaporn, D.; Chanlek, N.; Poo-Arporn, Y.; Mongkolthanaruk, W.; Eichhorn, S. J.; Pinitsoontorn, S. Carbon nanofiber aerogel/magnetic core-shell nanoparticle composites as recyclable oil sorbents. *ACS Appl. Nano Mater.* **2020**, *3*, 3939–3950.

[37] Alam, A.; Moussa, M. Preparation of graphene/poly(vinyl alcohol) composite hydrogel films with enhanced electrical and mechanical properties. *Polym. Compos.* **2020**, *41*, 809–816.

[38] Shi, Y.; Xiong, D. S.; Li, J. L.; Wang, N. The water-locking and cross-linking effects of graphene oxide on the load-bearing capacity of poly(vinyl alcohol) hydrogel. *RSC Adv.* **2016**, *6*, 82467–82477.

[39] Meng, Y. Q.; Zhao, X. W.; Ye, L. Construction of dual orientation crystalline structure in poly(vinyl alcohol)/graphene oxide nanocomposite hydrogels and reinforcing mechanism. *Ind. Eng. Chem. Res.* **2019**, *58*, 10908–10921.

[40] Li, R. N.; Zhang, L. Z.; Chen, T.; Wang, D. On-surface two-dimensional polymerization: Advances, challenges, and prospects. *Langmuir* **2023**, *39*, 12521–12532.

[41] Das, G. S.; Tripathi, K. M. Ecologically sustainable N-doped graphene nanosheets as high-performance electrodes for zinc-air batteries and zinc-ion supercapacitors. *ACS Appl. Electron. Mater.* **2024**, *6*, 1034–1044.

[42] Das, G. S.; Panigrahi, R.; Ghosh, S.; Tripathi, K. M. Waste frying oil derived carbon nano-onions as a cost-effective cathode material for high-voltage zinc-ion hybrid supercapacitors. *Mater. Today Sustain.* **2024**, *25*, 100656.

[43] Zhang, K. Q.; You, H. B.; Liu, Y. X.; Lin, F. L.; Li, Y. N.; Jia, L. N.; Bao, J. X.; Ge, X.; Pan, G. F.; Yu, H. T. et al. Development of a multifunctional and biocompatible hydrogel for flexible implantable sensors. *Chem. Eng. J.* **2025**, *522*, 167403.

[44] Han, S. W.; Tan, H. H.; Wei, J.; Yuan, H.; Li, S. W.; Yang, P. P.; Mi, H. Y.; Liu, C. T.; Shen, C. Y. Surface modification of super arborized silica for flexible and wearable ultrafast-response strain sensors with low hysteresis. *Adv. Sci.* **2023**, *10*, 2301713.

[45] Han, X. K.; Lu, T. Y.; Wang, H.; Zhang, Z. C.; Lu, S. R. Self-healing and freeze-resistant boat-fruited *Sterculia* seed polysaccharide/silk fiber hydrogel for wearable strain sensors. *ACS Sustain. Chem. Eng.* **2023**, *11*, 13756–13764.

[46] Fan, C. H.; Wang, D.; Huang, J. Y.; Ke, H. Z.; Wei, Q. F. A highly sensitive epidermal sensor based on triple-bonded hydrogels for strain/pressure sensing. *Compos. Commun.* **2021**, *28*, 100951.

[47] Peng, X. W.; Wang, W. D.; Yang, W. S.; Chen, J. S.; Peng, Q. Y.; Wang, T.; Yang, D. L.; Wang, J. M.; Zhang, H.; Zeng, H. B. Stretchable, compressible, and conductive hydrogel for sensitive wearable soft sensors. *J. Colloid Interface Sci.* **2022**, *618*, 111–120.

[48] Shao, L.; Li, Y.; Ma, Z. J.; Bai, Y.; Wang, J.; Zeng, P. Y.; Gong, P.; Shi, F. X.; Ji, Z. Y.; Qiao, Y. et al. Highly sensitive strain sensor based on a stretchable and conductive poly(vinyl alcohol)/phytic acid/NH_2-POSS hydrogel with a 3D microporous structure. *ACS Appl. Mater. Interface* **2020**, *12*, 26496–26508.

[49] Wang, B. Y.; Liu, W. X.; Liu, X. N.; Chen, D.; Song, Z. P.; Yu, D. H.; Li, G. D.; Wang, H. L.; Ge, S. H. Development of hierarchically constructed robust multifunctional hydrogels for sensitive strain sensors by using guar gum and polydopamine to encapsulate liquid metal droplets. *Appl. Mater. Today* **2023**, *35*, 101961.

[50] Zhang, R.; Liu, C. W.; Wei, C. M.; Wang, Y.; Li, F.; Zhang, Z. Q.; Qu, J. Q.; Qing, N.; Tang, L. Y. Thermoplastic charge-transfer hydrogels for highly sensitive strain and temperature sensors. *J. Mater. Chem. A* **2023**, *11*, 8320–8329.

[51] Zhang, Z. Y.; Yao, A. F.; Raffa, P. Transparent, highly stretchable, self-healing, adhesive, freezing-tolerant, and swelling-resistant multifunctional hydrogels for underwater motion detection and information transmission. *Adv. Funct. Mater.* **2024**, *34*, 2407529.